

Overview of simulation results using computation resources in the framework of IFERC-CSC

Duarte Borba^{1,2}, Atsushi Fukuyama³, Noriyoshi Nakajima⁴, Yasutomo Ishii⁴

¹EUROfusion Programme Management Unit, Culham Science Center, Abingdon, OX14 3DB, UK, ²Instituto de Plasmas e Fusão Nuclear, Instituto Superior Técnico, Av Rovisco Pais Lisboa, Portugal, ³Kyoto University, Kyoto-Daigaku-Katsura C3, Nishikyo-ku, Kyoto 615-8540, JAPAN, ⁴IFERC, 2-166 Rokkasho, Aomori 039-3212, Japan

Abstract

Following the successful operation of a European High Performance Computer For Fusion applications (HPC-FF) in Jülich, Germany, from 2009 to 2013, a new supercomputer dedicated to magnetic fusion research was procured within the Broader Approach agreement between Europe and Japan. The new platform, “Helios”, was installed in the International Fusion Energy Research Centre - Computational Simulation Centre (IFERC-CSC) in Rokkasho, Japan and it started operations in January 2012 and is expected to serve until the end of 2016. The computer was purchased within the Broader Approach agreement between the EU and Japan managed by Fusion for Energy, as an in kind contribution by France provided by CEA. In this paper, the main scientific and technical results obtained in the Helios numerical simulations projects are described with emphasis on the impact in developing fusion science and related technologies. At the end of its life cycle the use of Helios will be replaced in Europe with a new EUROfusion supercomputer, allowing further development of fusion technologies based on computer modelling and simulations. Collaborations between Japan and Europe will continue with new opportunities for joint projects like Helios.

Introduction

The main configuration of Helios includes 9000 INTEL Sandy-Bridge EP processors with a total of 72000 cores (1550 TFlops) and 360 INTEL Xeon Phi 5110P processors with a total of 21600 cores (412 TFlops). The operation of Helios has been organised in 5 yearly cycles, open to projects led by scientists and engineers of fusion research organisations in EU or Japan and open to all fusion researchers covered by a formal agreement with the respective EU or Japan institution leading the project (figure 1); and focus on large scale simulation activities to analyse experimental data on fusion plasmas, prepare scenarios for ITER operation, predict the performance of ITER, and contribute to DEMO design physics basis and Broader Approach activities. The Helios numerical simulations projects covers mainly: plasma turbulence and related transport processes, fast particle physics, linear, nonlinear and/or extended Magneto-Hydro-Dynamic (MHD), edge physics, heating and current drive, integrated modelling of fusion plasmas, development of reactor materials and reactor technologies, together with the associated developments of better numerical schemes and parallelization of algorithms with general applications to computation science, such as the development of a Parallel Multigrid Solver on a Structured Triangulation of a Hexagonal Domain (1).

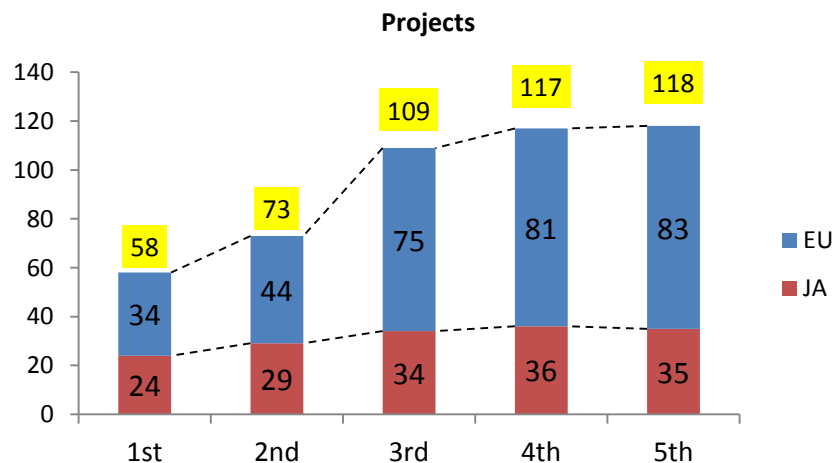


Figure 1 Number of projects run in the Helios computer through the five yearly cycles

Development of improved numerical schemes

A number of novel numerical techniques have been developed and tested on Helios. The developments focussed mainly on noise reduction in particle in cell based algorithms and improvements in the collision operators. Development of improved numerical schemes in modern gyrokinetic theory was implemented on GT5D (2) up to third order accuracy in the gyrokinetic ordering, and the toroidal angular momentum conservation in a full-f gyrokinetic model was verified.

Computation overlap techniques and multi-layer domain decomposition techniques were also developed in GT5D (3) and an excellent strong scaling up to the Helios full system was shown (4). Noise reduction efforts included the development of a new radially local neoclassical transport code based on the radially global two-weight δf Monte Carlo code, FORTEC-3D (5). In the collisional two-weight δf method, the variance of weight increases in time due to the so-called weight spreading, which leads to an increasing numerical noise in simulations spanning long periods of time. A new improved control-variate scheme was proposed by

(6) to reduce the variance. It was demonstrated that the new scheme reduces the variance of weight by approximately 75% in an axisymmetric magnetic field configuration (7). An algorithm for exact gyro-density transport has been developed, and it was shown to allow accurate simulations with an order of magnitude fewer markers (8). The effects of cloud-in-cell sampling and gyro-averaging on random noise in real space (as opposed to the common Fourier space presentation) was studied, and it was shown that together, these can reduce the noise by a factor of 3 compared to nearest grid point sampling without gyro-averaging. Hence an order of magnitude less test particles are needed for a given noise level (9). A new linearized collision operator, which preserves the conservation properties of particles, momentum, and energy, and the self-adjointness relation for arbitrary particle species, was applied to Eulerian kinetic simulations of multi-species ions and electrons. It was confirmed that the modified collision operator successfully reproduces the collisional relaxation of multi-species ions and electrons towards their equilibrium distributions satisfying the self-adjointness relation (10) (11). In the same vein, a novel linearized multi-species collision operator has been proposed for full-f gyrokinetic codes and successfully tested with GYSELA (12). Two different versions of a discrete parallel diffusion operator were derived and tested. The first is based on interpolation where the order of interpolation and therefore the numerical diffusion is adjustable; the second is based on integration and is advantageous in cases where the field line map is strongly distorted (13). In addition, a new algorithm for electromagnetic gyrokinetic simulations, the so called “pullback transformation scheme” proposed by (14) motivated as an explicit time integrator reset after each full time-step was investigated in detail. Using a numerical dispersion relation valid in slab geometry, it is shown that the linear properties of the scheme are comparable to those of an implicit parallel velocity-scheme (15). Numerical techniques for parallel dynamics in electromagnetic gyrokinetic simulations were introduced to regulate unphysical grid-size oscillations in the field-aligned coordinate (16). In addition, curvilinear guiding-centre drift and full-orbit equations of motion were implemented and tested in the VENUS-LEVIS code (17). Recently up to five codes (GENE, GKW, ORB5, EUTERPE, GYSELA) joined a gyrokinetic global code benchmark that ultimately shows agreement of Eulerian and PIC based codes on electromagnetic micro instabilities (18).

Plasma turbulence and related transport processes

Plasma turbulence simulations have moved towards full torus calculations and the inclusion of more sophisticated models for the electromagnetic effects, real ion-to-electron mass ratio, role of fast ions, momentum transport, the role of Geodesic Acoustic modes, electron dynamics and three dimensional (3D) effects with applications to Tokamaks and Stellarators; with more detailed comparisons with experimental data of experiments such as JET, JT-60U, DIII-D, ASDEX-Upgrade, MAST, Tore Supra and FT2 tokamaks; and W7X, LHD, TJ-II stellarators, together with predictive simulations of future devices such as JT-60SA and ITER. Detailed examination of the mechanisms whereby magnetic stochasticity and transport develop in electromagnetic ion-temperature-gradient (ITG)-driven turbulence was carried out. This work explains many of the features of electromagnetic micro-turbulence discovered in recent gyrokinetic studies and may offer a paradigm, which can be examined in a broader range of parameter regimes, for how magnetic fluctuations develop in turbulence driven by instabilities that are not intrinsically electromagnetic (19). The kinetic ballooning mode (KBM) turbulence in Tokamak plasma was investigated by electromagnetic gyrokinetic simulations. From the entropy balance analysis, it is revealed that the field-particle interactions transfer a significant fraction of the ion entropy produced by the instability to electrons. Then, the produced ion entropy balances the sum of the ion and electron dissipations at the saturation of the KBM instability growth, in contrast to ITG turbulence where ion entropy production mostly balances the ion dissipation. (20). Analysis of turbulent fluxes, norms, and phases of fluctuations in high- β plasmas with the local gyrokinetic model shows that KBM turbulence gives narrower spectra and smaller phase factors than those in ITG-driven turbulence (21). Multiscale gyrokinetic turbulence simulations with the real ion-to-electron mass ratio and β value were carried out for the first time. Numerical analysis at both the electron scale and the ion scale reveals the mechanism of their cross-scale interactions. Even with the real mass scale separation, ion-scale turbulence may eliminate electron-scale streamers and dominates heat transport, not only of ions but also of electrons. Suppression of electron-scale turbulence by ion-scale eddies, rather than by long-wavelength zonal flows, is also demonstrated by means of direct measurement of nonlinear mode-to-mode coupling. When the ion-scale modes are stabilized by finite- β effects, the contribution of the electron-scale dynamics to the turbulent transport becomes non-negligible and turns out to enhance ion-scale turbulent transport. Damping of the ion-scale zonal flows by electron-scale turbulence is responsible for the enhancement of ion-scale transport (figure 3) (22). The response of high-energy alpha particles to electrostatic turbulence has been analysed for several different tokamak parameters. The results confirmed that the effect of alphas on the turbulence is negligible at realistically low concentrations, consistent with linear theory (23). Simulations of Kinetic Electrostatic Electron Nonlinear (KEEN) Waves, (non-stationary, nonlinear, self-organized asymptotic states in Vlasov plasmas), with Variable Velocity Resolution Grids and High-Order Time-Splitting were performed (figure 2). Newly discovered features of the dynamics of KEEN waves include the finite partitioning of phase space, unusual particle orbit statistics variations in the topology near separatrices for weak to strong drive, successive harmonic generation instabilities and phase locking (24). Global gyrokinetic simulations of electrostatic temperature-gradient-driven trapped-electron-mode (TEM) turbulence were performed using the δf particle-in-cell global gyrokinetic particle-in-cell code ORB5. The electron response is either fully kinetic or hybrid, i.e. considering kinetic trapped and adiabatic passing electrons. Electron collisions are found to damp TEMs through the detrapping process, while finite larmor radius effects turn out to be important in the non-linear regime but very small in the linear regime (25). A new hybrid kinetic electron model, which keeps important physics such as the ITG-TEM, the neoclassical transport, the ambipolar condition, and particle trapping and detrapping processes, was developed (26), and long time full-f gyrokinetic simulations of the ITG-TEM turbulence were enabled. Decaying ITG turbulence simulations with adiabatic and kinetic electrons were compared, and it was found that in the latter, corrugated density profiles, which are produced by electrons transport near mode rational surfaces, generate microscopic radial electric fields, and suppress the ITG turbulence (27). Using the ORB5 code with the adiabatic electron model, it was observed that long-lived zonal flow structures, leading to a corrugated transport and temperature gradient pattern, could develop in shaped tokamak plasmas much more than in circular shaped plasmas, resulting in reduced transport. The hybrid electron model confirms the results of the fully adiabatic electron model. Results show the presence of large radial zones straddling the core-pedestal transition region. Avalanche-like events propagate over the radial zone at constant speed and repeat with a well-defined frequency somewhat below the local geodesic acoustic mode (GAM) frequency (28). Turbulent transport caused by electron temperature gradient (ETG) modes was investigated by means of gyrokinetic simulations. It was found that the ETG turbulence can be regulated by meso-scale zonal flows driven by TEM,

which are excited with much smaller growth rates than those of ETG modes. The zonal flows of which radial wavelengths are in between the ion and the electron banana widths are not shielded by trapped ions nor electrons, and hence they are effectively driven by the TEMs. It was also shown that an ExB shearing rate of the TEM-driven zonal flows is larger than or comparable to the growth rates of long-wavelength ETG modes and TEMs, which make a main contribution to the turbulent transport before excitation of the zonal flows (29). Comparison between the ITG and ETG cases shows that ETG turbulence has a more pronounced classical turbulent behaviour, exhibiting a stronger energy cascade, with implications for gyrokinetic turbulence modelling (30). The response of passing electrons in ion temperature gradient and trapped electron mode microturbulence regimes was investigated in tokamak geometry making use of the flux-tube version of the gyrokinetic code GENE. Comparing linear eigenmodes obtained enables to systematically isolate fine radial structures located at corresponding mode rational surfaces, clearly resulting from the non-adiabatic passing-electron response. Non-linear simulations show that these fine structures on the non-axisymmetric modes survive in the turbulent phase (31). The effect of the tangential magnetic drift on the local neoclassical transport was investigated. It was demonstrated that the effect of the drift is negligible for the neoclassical transport in tokamaks. In non-axisymmetric systems, however, the tangential magnetic drift substantially changes the dependence of the neoclassical transport on the radial electric field (32). The simulation study of nonlocal transport from edge to core in tokamak plasmas was performed using the 4-field reduced MHD model. It was shown that the convective cell modes contribute the nonlocal transport, indicating that 2D transport plays an essential role to produce the nonlocal transport (33) (34). ITG driven turbulence simulation for a transient edge temperature sink localized in the poloidal plane was performed using a global Landau-fluid code in the electrostatic limit. Simulations showed that the ITG turbulence in the core region dissipates the large-scale perturbations and weakens the edge-core connection (35). A new simulation method for local turbulence in toroidal plasmas was developed by extending the conventional idea of the flux tube model. In the new approach, a train of flux tubes is employed, where flux tube simulation boxes are serially connected at each end along a field line so as to preserve the symmetry of the local gyrokinetic equations for modes in an axisymmetric torus (36). Poloidal tilting symmetry of the local nonlinear δf gyrokinetic model was demonstrated analytically and verified numerically. This symmetry shows that poloidally rotating all the flux surface shaping effects with large poloidal mode number by a single tilt angle has an exponentially small effect on the transport properties of a tokamak (37). It has been demonstrated that breaking the up-down symmetry of tokamak flux surfaces removes a constraint that limits intrinsic momentum transport, and hence toroidal rotation. It was shown, through MHD analysis, that ellipticity is most effective at introducing up-down asymmetry throughout the plasma. Though other known core intrinsic momentum transport mechanisms scale poorly to larger machines, these results indicate that up-down asymmetry may be a feasible method to generate the current experimentally measured rotation levels in reactor-sized devices (38). A mechanism to keep steady intrinsic rotation was studied based on the toroidal angular momentum conservation in a confinement time scale full-f simulation. It was found that in the steady state, the turbulent stress induced by bursty ITG turbulence is cancelled by the neoclassical counterpart, which is enhanced in the presence of asymmetric turbulent fluctuations (39). The physics underlying the non-zonal transition (40) were explored in detail and the results obtained support the theory that critically weakened zonal flows are indeed responsible for the failure of ion-temperature gradient-driven turbulence at high plasma β to saturate at typical transport values (41). Plasma turbulence and related transport processes, in addition to a full-f fixed-flux model, a delta-f like fixed-gradient model was implemented in GT5D, and detailed physics comparisons of turbulence properties in fixed-flux, fixed-gradient, and flux-tube models were shown. The comparison revealed a mechanism of bursty transport leading to a Bohm like transport in a fixed-flux model (42). A plasma size scan was performed up to $1/\rho^* \sim 600$ using the GT5D, and it was shown that, when the heating power is scaled with the plasma size, the plasma size scaling is affected by the power degradation of the confinement and a Bohm-like feature persists even at large plasma sizes, where delta-f simulations predict a gyro-Bohm scaling (43). Global simulations of collisional ITG-driven microturbulence were performed with the nonlinear global gyrokinetic code GENE, comparing systems with and without neoclassical effects. In fixed-gradient simulations, the modified radial electric field is shown to alter the zonal flow pattern such that a significant increase in turbulent transport is observed and the dependency of the flux on the collisionality changes. In simulations with fixed power input, the presence of neoclassical effects decreases the frequency and amplitude of intermittent turbulent transport bursts (avalanches) and thus plays an important role for the self-organisation behaviour (44). The possible control of turbulence has been explored with the flux-driven GYSELA code. Polarizing locally the plasma by means of a vorticity source, mimicking some experimental scenarios, has proven efficient in triggering a transport barrier, which appears to relax quasi-periodically (45). These relaxations turn out to result from the decoupling between the dynamics of the barrier generation, governed by the source driven sheared flow, and that of the crash, triggered by a secondary instability. Also, the interplay between Energetic particle geodesic acoustic modes (EGAMs) and turbulence has been studied. The excitation of EGAMs in a regime with a transport barrier in the outer radial region has led to an increase of turbulent transport, with the subsequent destruction of the transport barrier (46). The global eigenmode structures of linear ITG modes in tokamak plasmas were obtained using a novel technique which combines results from the local gyrokinetic code GS2 with analytical theory to reconstruct global properties. Toroidal flow shear, introduced as a Doppler shift in the real frequency, also influences the global mode. Moreover, flow shear is also found to shift the mode radially. For a critical flow shear the isolated mode can exist even with arbitrary profiles. (47). The relation between the ITG turbulence, zonal flows, and the transport in helical plasmas was investigated by nonlinear gyrokinetic simulations. Local gyrokinetic simulations for 3D helical field configurations were carried out employing various parameters such as the density and temperature gradients and local shears. From the simulation results, a simple model function to represent ion heat diffusivity in terms of the turbulent fluctuations and zonal flow amplitude in helical plasmas was constructed (48). 3D MHD numerical simulations, of the nonlinear excitation of a large scale magnetic island and its dynamical properties due to the presence of small-scale turbulence was investigated. It was found that quasi-resonant localized interchange modes at the plasma edge can beat together and produce extended modes that transfer energy to the lowest order resonant surface in an inner stable zone and induce a seed magnetic island (49). Turbulence induced by the ITG was investigated in the helical and axisymmetric plasma states of a reversed field pinch device by means of gyrokinetic calculations. The two magnetic configurations were systematically compared, both linearly and nonlinearly, in order to evaluate the impact of the geometry on the instability and its ensuing transport, as well as on the production of zonal flows. Despite its enhanced confinement, the high-current helical state demonstrates a lower ITG stability threshold compared to the axisymmetric state, and ITG turbulence is expected to become an important contributor to the total heat transport (50). Experimental discharges with pulsed poloidal current drive (PPCD) in the Madison Symmetric Torus reversed field pinch were investigated using a semi-analytic equilibrium model in the gyrokinetic turbulence code GENE. Relative to expectations of tokamak core plasmas, the

critical gradients for the onset of these instabilities are found to be greater by roughly a factor of the aspect ratio. A significant upshift in the nonlinear TEM transport threshold, previously found for tokamaks, is confirmed in nonlinear reversed field pinch simulations and is roughly three times the threshold for linear instability (51). A saturation mechanism for microturbulence in a regime of weak zonal flow generation was investigated by means of electromagnetic gyrokinetic simulations. A new saturation process of the kinetic ballooning mode (KBM) turbulence originating from the spatial structure of the KBM instabilities in a finite- β Large Helical Device (LHD) plasma was identified (52). The inclusion of kinetic electrons in the models enabled the evaluation of the particle and the electron heat fluxes caused by turbulence in LHD plasmas. It was found that the electron energy transport reproduces the experimental results and that the critical gradient for turbulent energy flux is similar to that for the linear instability, i.e., the Dimits shift is small. This is because the zonal flow in LHD is weaker than that in tokamaks (53). The very first simulations of ITG turbulence on the W7X surface revealed a strong localization of fluctuations and a milder transport stiffness compared to a tokamak. Gyrokinetic simulations were used to predict the distribution of turbulence fluctuations and the related transport scaling on entire stellarator magnetic surfaces, revealing striking differences to tokamaks. Using a stochastic global-search optimization method, the first turbulence-optimized stellarator configuration was obtained stemming from an existing quasisymmetric design (54). Simulations of plasma turbulence revealed also that stellarators possess two intrinsic mechanisms to mitigate the effect of the drive generated by the locally compressed regions obtained in the modern carefully optimized shaped stellarators. In the regime where the length scale of the turbulence is very small compared to the equilibrium scale set by the variation of the magnetic field, the strongest fluctuations form narrow bandlike structures on the magnetic surfaces. Thanks to this localization, the average transport through the surface is significantly smaller than that predicted at locations of peak turbulence. In a second regime lacking scale separation, the localization is lost and the fluctuations spread out on the magnetic surface. Nonetheless, stabilization persists through the suppression of the large eddies (relative to the equilibrium scale), leading to a reduced stiffness for the heat flux dependence on the ion temperature gradient (55). Particle transport after injection of a pellet in the TJ-II stellarator was simulated with the code FORTEC-3D, obtaining good agreement with the experimental measurements; it was shown that the change in neoclassical transport caused by the pellet is able to fuel the plasma core (56). The stability properties of W7X and a more quasi-isodynamic configuration, QIPC, were investigated numerically and compared with the National Compact Stellarator Experiment and the DIII-D tokamak using gyrokinetic simulations performed with GENE in the electrostatic and collisionless approximation. ITG modes, TEM, and mixed-type instabilities were studied. W7X and QIPC exhibit significantly reduced growth rates for all simulations that include kinetic electrons, suggesting a weaker TEM transport than a shaped tokamak, due to quasi-isodynamicity (57). Neoclassical Monte Carlo simulations of the direct observations of electrostatic potential variations along the flux surfaces of the TJ-II stellarator were able to estimate the correct order of magnitude for the overall variation in potential and predict the trend observed with the radial electric field (58). The impact of electromagnetic stabilization and flow shear stabilization on ITG turbulence was investigated. The analysis of a low- β JET L-mode discharge illustrates the relation between ITG stabilization and proximity to the electromagnetic instability threshold. This threshold is reduced by suprathreshold pressure gradients, highlighting the effectiveness of fast ions in ITG stabilization (59). Extensive linear and non-linear gyrokinetic simulations and linear MHD analyses performed for JET hybrid discharges with improved confinement have shown that the large population of fast ions found in the plasma core under particular heating conditions has a strong impact on core microturbulence and edge MHD by reducing core ion heat fluxes and increasing pedestal pressure in a feedback mechanism. In the case of the JET metal ITER-like wall (ILW), it was shown how this mechanism plays a decisive role for the transition to plasma regimes with improved confinement and it can explain the weak power degradation obtained in dedicated power scans. The mechanism is found to be highly dependent on plasma triangularity as it changes the balance between the improvement in the plasma core and the edge (60). Analysis of the deterioration of global confinement in the ILW has been carried out using the gyrokinetic code GENE. The core ion energy confinement time was found to be comparable to the Carbon scenarios, while the electron confinement time is shorter for the ILW discharges (61). Previous nonlinear gyrokinetic simulations of specific DIII-D L-mode cases have been found to significantly under predict the ion heat transport and associated density and temperature fluctuation levels by up to almost one order of magnitude in the outer-core domain, i.e., roughly in the last third of the minor radius. Contrary to the previous studies, new simulations of plasma micro-turbulence with the code GENE applied to one of the L-mode discharges showed only a mild under prediction at the outer radial positions which can furthermore be overcome by varying the ion temperature gradient within the error bars associated with the experimental measurements (62) (63). ASDEX Upgrade discharges were modelled using the GENE code by analysing various fluctuating quantities and comparing them to experimental measurements. It was found that density and temperature fluctuations can vary significantly with small changes in the parameters, thus making comparisons with experiments very sensitive to uncertainties in the experimental profiles. However, cross-phases are more robust, indicating that they are better observables for comparisons between gyrokinetic simulations and experimental measurements (64). Using the highly accurate measurements at ASDEX Upgrade, the GENE turbulence code was also used to perform a comprehensive gyrokinetic study of dedicated H-Mode plasmas. It was found that the stabilization of ITG driven turbulence to be the most pronounced β effect in these experimentally relevant cases. The resulting β -improved core confinement should thus be considered for extrapolations to future machines (65). The gyrokinetic GENE code was used to study the inter-edge localized mode (ELM) H-mode pedestal profile evolution for an ASDEX Upgrade discharge. Density gradient driven trapped electron modes are the dominant pedestal instability during the early density-build up phase. Nonlinear simulations produce particle transport levels consistent with experimental expectations. Later inter-ELM phases appear to be simultaneously constrained by ETG and kinetic ballooning mode (KBM) turbulence (66). Turbulence in hot magnetized plasmas is shown to generate permeable localized transport barriers that globally organize into the so-called "ExB staircase" (67). Based on turbulence computations with GYSELA and theoretical predictions, staircases are observed experimentally in the Tore Supra tokamak by means of high-resolution fast-sweeping X-mode reflectometry. This observation strongly emphasizes the critical role of mesoscale self-organization in plasma turbulence and may have far-reaching consequences for turbulent transport models and their validation (68). The experimental observation made on the TCV tokamak of a significant confinement improvement in plasmas with negative triangularity was compared to those with standard positive triangularity and has been interpreted in terms of different degrees of profile stiffness and/or different critical gradients. Employing the Eulerian gyrokinetic code GENE, profile stiffness and critical gradients were studied under TCV relevant conditions. The importance of considering the sensitivity to both temperature and density gradient is shown. The flux tube results show an increase of the critical gradients towards the edge, further enhanced for negative triangularity, and they also appear to indicate a reduction of profile stiffness towards the plasma edge (69). A comparative investigation of the

isotope effect in multi-scale anomalous transport phenomena is performed both experimentally by highly localized turbulence diagnostics in comparable H and deuterium FT-2 tokamak discharges and theoretically with the help of global gyrokinetic modeling. The substantial excess of the GAM amplitude, radial wavelength and correlation length in a wide spatial region in deuterium discharges, resulting in stronger modulation of drift-wave turbulence level is demonstrated by both approaches (70) (71). The gyrokinetic full 5D particle distribution code ELMFIRE has been extended to simulate circular tokamak plasmas from the magnetic axis to the limiter Scrape off Layer (SOL). The predictive power of the code in the full torus configuration was tested via its ability to reproduce experimental steady-state profiles in FT-2 ohmic L-mode plasmas. The results show that the experimental profile solution is not reproduced numerically due to the difficulty of obtaining global power balance (72). The radial electric field dynamics was studied in gyrokinetic full-f simulations of tokamak plasmas. The calculations used parameters similar to a TEXTOR L-mode discharge in the presence of a steep density gradient and dominating trapped electron mode turbulence in the edge pedestal of the plasma. Temperature, density gradient and ion species are varied to study the radial electric field fluctuations and their relationship with thermal transport. The dominant frequency of electric field oscillations is within the geodesic acoustic mode range, and their amplitude is found to be clearly correlated with transport across the parametric scan (73). Measurements of local density and magnetic field fluctuations near the pedestal top, conditionally averaged over the ELM cycle, have been made in MAST. Linear GS2 calculations show that both microtearing modes (MTMs) and ETG modes are unstable with similar wave numbers as the measurements at the top of the pedestal, along with kinetic ballooning modes that are unstable lower in the pedestal at larger wavelengths. Both the experimental wave number range and the fluctuation ratio are more similar to the linear characteristics of the ETG than the MTM. These results imply that intermediate-wave length fluctuations due to the ETG play a role in inter-ELM pedestal evolution (74). It was shown that for parameters typical for Spherical Tokamak discharges with reversed shear profiles and with large enough field line pitch, a robust spontaneous symmetry breaking occurs, leading to the generation of strong toroidal flow structures (75). An experimental regime with no confinement degradation during Electron Cyclotron Resonant Heating (ECRH) has been identified using data in a wide operating regime, positive magnetic shear, weak magnetic shear and reversed magnetic shear plasmas on JT-60U with the help of local gyrokinetic flux-tube code GS2 calculations of the fastest growing modes (76). Global gyrokinetic simulations of ITG driven turbulence for ITER were performed with the ORB5 code. A self-organized radial structure appears, with long-lived Zonal Flows (ZF), modulating turbulence heat transport and resulting in a corrugated temperature gradient profile. The ratio of long-lived ZF to the fluctuating ZF is markedly higher for ITER as compared with circular configurations, thereby producing a more effective ITG turbulence suppression, in spite of a higher linear growth rate (77). The current ramp-up with reduced central solenoid flux consumption in JT-60SA has been investigated using an integrated modelling code suite TOPICS with a turbulent model CDBM. The results show that the plasma current can be ramped-up from 0.6 MA to 2.1 MA with no additional central solenoid flux consumption if the plasma current is overdriven by the neutral beams and bootstrap current. The duration required for the current ramp-up without central solenoid flux consumption becomes as long as 150 seconds in this scenario (78).

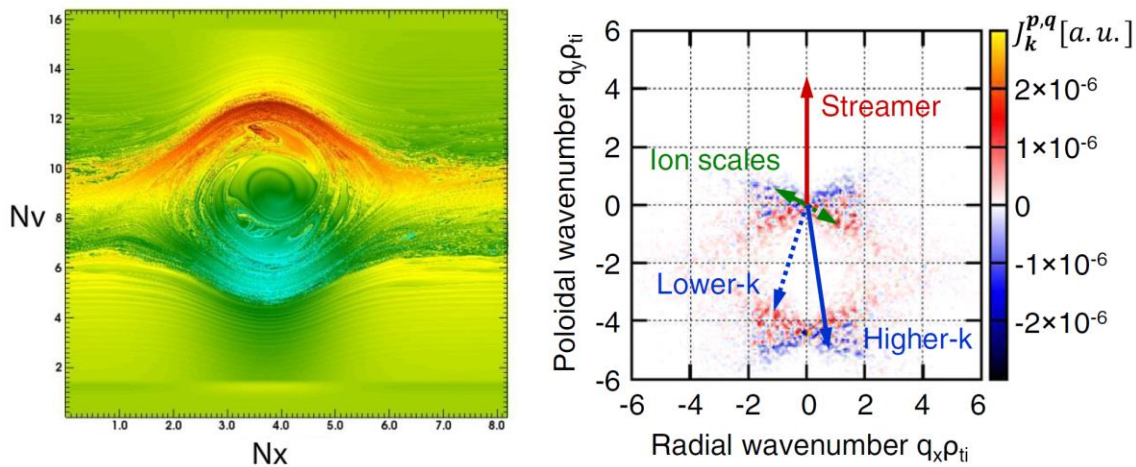


Figure 2 δf distribution function of Kinetic Electrostatic Electron Nonlinear (KEEN) Waves, non-stationary, nonlinear, self-organized asymptotic states in Vlasov plasmas (79), in a the 2D phase space (N_x, N_v) refined grid. Figure 3 Wave number spectrum of the triad transfer for a typical streamer in cross-scale Interactions between Electron and Ion Scale Turbulence simulations in a Tokamak Plasmas. The arrows represent dominant triad couplings (80).

Edge Physics

The new SOLPS-ITER code package has been developed and applied for detailed benchmarking of ITER divertor design studies exploiting the MPI parallelisation techniques of the EIRENE neutral Monte-Carlo code (81). Turbulence simulations have clarified the relative role of the resistive ballooning modes, drift waves, and ITG modes in the SOL. The statistical properties of turbulence have been studied, together with the propagation of blobs. The effect of neutrals has been incorporated in the models and the origin and nature of intrinsic toroidal plasma rotation in the SOL was investigated as well as the oscillation modes in the plasma sheath. The simulation results have been confronted with experiments from several devices such as TORPEX, Alcator C-mod, JT-60U and JET. The models developed were used to predict the behaviour of the SOL in future devices such as ITER and DEMO.

Analysis, based on the linear electrostatic drift-reduced Braginskii equations, identified the non-linear turbulent regimes in the tokamak SOL according to the linear instability responsible for the perpendicular transport. Four regions of the SOL operational parameters were determined where turbulence is driven by the inertial or resistive branches of the ballooning mode or of drift waves (82). Detailed analysis of finite ion temperature effects on the linear SOL instabilities, such as the resistive and inertial branches of drift waves and ballooning modes, revealed that the ITG plays a negligible role in limited SOL discharges, since the ITG is generally

below the threshold for driving the mode unstable (83). Simulations describing turbulence in the tokamak SOL were carried out with the global, flux-driven fluid 3D drift-reduced Braginskii code GBS (84). Linearly, both simulations and simplified analytical models reveal a stabilization of ballooning modes. Nonlinearly, flux-driven nonlinear simulations give a pressure characteristic length whose trends are correctly captured by the gradient removal theory (85), that assumes the profile flattening from the linear modes as the saturation mechanism. More specifically, the linear stabilization of ballooning modes is reflected by a 15% increase in the steady-state pressure gradient obtained from GBS nonlinear simulations when going from an infinite to a realistic aspect ratio (86). The statistical properties of turbulent physical fields such as density, electrostatic potential, and temperature, focusing on the mathematical expression of tails of the probability distribution functions were generated from time-traces of the plasma density stemming from Braginskii-type fluid simulations and checked against first-principles theoretical models. The analysis of the numerical simulations indicates that the probability distribution function of the intermittent process contains strong exponential tails, as predicted by the analytical theory (87). The propagation of blobs, structures of localized enhanced plasma pressure, was studied in global 3D simulations of a simple magnetized torus. In particular, single-seeded blob simulations were carried out to explore the dependence of the blob velocity with respect to its size. It is found that the velocity scaling for two-dimensional blobs is satisfied in the parameter space where polarization currents are the dominant damping mechanism (88). 3D and 2D seeded blob simulations were performed with five different fluid models, all based on the drift-reduced Braginskii equations, and the numerical results were compared among themselves and validated against experimental measurements provided by the TORPEX device (89). The comparisons demonstrate that the radial blob dynamics observed in the 3D simulations is in good agreement with experimental measurements. Moreover, it was found that an accurate measurement of the blob temperature is important to perform reliable seeded blob simulations (90). A quantitative comparison between gas-puff imaging (GPI) turbulence measurements in Alcator C-Mod inner-wall limited discharges (91) and 3D flux-driven drift-reduced Braginskii turbulence simulations of SOL dynamics were carried out. The comparison between GPI data and non-linear simulations yields overall good agreement for several observables, such as the $D\alpha$ emission levels and intermittency, the radial and poloidal correlation lengths and propagation velocities, and the power and frequency spectral density (92). Simulations of the W prompt re-deposition processes at the divertor plates via kinetic modelling of the JET SOL for different divertor plasma parameters demonstrated that the electric field and not the Lorentz Force is the major contributor to the prompt re-deposition process (93). Using the kinetic description of the plasma, the stability of the potential shape in the quasi-neutral pre-sheath with respect to the high and low frequency perturbations was investigated. Regarding high-frequency perturbations, the pre-sheath is shown to be stable. It was also shown that the stability problem related to low-frequency perturbations can be reduced to an analysis of a “diffusion like” equation (94). A theory-based scaling for the characteristic length of a circular, limited tokamak SOL is obtained by considering the balance between parallel losses and non-linearly saturated resistive ballooning mode turbulence, providing an estimate for the ITER start-up phase (95). The integrated divertor code SONIC has been used to model the JT-60U detached divertor plasma. In this study, the radial diffusion coefficient in the private region or the far SOL region is increased to investigate the influence of radial plasma transport on detachment characteristics. Saturation of the reduction in ion flux after roll-over is improved by the radial transport enhancement, while the radial profile at the mid-plane agreed with the experimental data (96). The power exhaust for a 3GW fusion reactor with an ITER-sized plasma was investigated by enhancing the radiation loss from seeding impurities. The impurity transport and plasma detachment were simulated under the DEMO divertor condition using the integrated divertor code SONIC. Results for the different seeding impurities showed that the total heat load, including the plasma transport and radiation was reduced from 16 MWm^{-2} with Ne and Ar (97) to 11 MWm^{-2} for the higher Z (Kr) impurities, and the radiation load extended over a wide area accompanied by increased impurity recycling (figure 4) (98).

A first-principles self-consistent model that couples plasma and neutral physics suitable for the simulation of turbulent plasma behavior in the tokamak SOL was developed. While the plasma is modelled by the drift-reduced two fluid Braginskii equations, a kinetic model for the neutrals was developed, valid in short and in long mean free path scenarios (99). The implementation of the self-consistent model of plasma recombination into the fully kinetic massively parallel Particle-in-Cell/Monte Carlo BIT1 PIC code and the simulations of detached SOL plasmas indicate that in a strongly recombining plasma edge the sheath properties do not change qualitatively. The most affected parameter is the sheath heat transmission coefficient, which can increase by an order of magnitude (100). The origin and nature of intrinsic toroidal plasma rotation in the SOL of tokamaks was investigated both analytically and through numerical simulations. It was shown that the equilibrium poloidal ExB flow, the sheath physics, and the presence of poloidal asymmetries in the pressure profile act as sources of momentum, while turbulence provides the mechanism for the radial momentum transport (101). In addition, different plasma oscillation modes in the plasma sheath (PS) have been studied with the code BIT1. The largest oscillation amplitudes are the waves which are in resonance with the local plasma frequency for unmagnetized, and with the upper and lower hybrid frequencies for magnetized plasmas (102).

Linear, nonlinear and/or extended Magneto-Hydro-Dynamic (MHD)

MHD simulations focussed on the study of edge localized modes (ELM), disruptions and generation of runaway electrons, together with the analysis of kink, peeling and ballooning modes, Rayleigh-Taylor instabilities, microtearing modes (MTMs), tearing modes, collisionless magnetic reconnection and neoclassical toroidal viscosity (NTV). ELM studies are at a very mature level of sophistication, being able to reproduce complete ELM cycles and also showing a mechanism for resonant magnetic perturbations (RMPs) and pellet ELM control in collisional plasmas.

An analytic solution for the expansion of a plasma into vacuum was assessed for its relevance to the parallel transport of ELM filaments along field lines. This solution solves the 1D Vlasov–Poisson equations for the adiabatic (instantaneous source), collisionless expansion of a Gaussian plasma bunch into an infinite space in the quasineutral limit. Importantly, the analytic solution predicts a zero heat flux density so that a fluid approach to the problem can be used equally well, at least when the source is instantaneous. It was found that, even for JET-like pedestal parameters, collisions can affect the expansion dynamics via electron temperature isotropisation (103). Nonlinear simulations of the early ELM phase based on a typical type-I ELMy ASDEX Upgrade discharge have been carried out using the non-linear resistive reduce MHD code JOEKE. The analysis focused on the evolution of the toroidal Fourier spectrum. It was found that during the nonlinear evolution, linearly subdominant low- n Fourier components, in particular the $n=1$, grow to energies comparable with linearly dominant harmonics (104). The mechanisms of the ELM energy deposition were studied by means of non-linear MHD simulation of ELMs. The footprint of the ELM heat flux at the divertor is

found to increase approximately linearly with the total ELM energy loss for JET-scale plasmas, which is similar to the experimentally observed broadening of the ELM energy deposition with ELM energy loss (105). The interaction of static RMPs with the plasma flow was modelled in toroidal geometry, using the code JOREK, which includes the X-point and the SOL. Two-fluid diamagnetic effects, the neoclassical poloidal friction and a source of toroidal rotation are introduced in the model to describe realistic plasma flows. For JET-like parameters, three regimes of the plasma response were found depending on the plasma resistivity and the diamagnetic rotation. In MAST Double Null Divertor geometries, lobes are found near the X-point and the 3D-deformation of the density and temperature profiles were observed (106). The dynamics of multi-ELM cycle as well as the ELM mitigation by RMPs were modelled in realistic tokamak X-point geometry with the code JOREK. The diamagnetic rotation is found to be a key parameter enabling to reproduce the cyclical dynamics of the plasma relaxations and to model the near-symmetric ELM power deposition on the inner and outer divertor target plates consistently with experimental measurements (107) (108). Simulations of ELM filament dynamics in MAST double-null plasmas were compared with experimental observations (109). Divertor heat flux measurements from JET ITER-like wall (ILW) discharges were used in quantitative comparisons with simulations, highlighting the importance of pre-ELM equilibria and parallel energy transport models in MHD simulations (110). A possible mechanism of ELM mitigation by RMP was proposed based on the results using the JOREK code. Realistic JET-like plasma parameters and an RMP spectrum of the JET error-field correction coils (EFCC) with a main toroidal number $n=2$ were used in the simulations, which reproduces the generic features of high collisionality RMP experiments (111). It is known that mitigating ELM with RMPs can increase energetic particle losses and resulting wall loads, which have previously been studied in the vacuum approximation. Recent results of fusion alpha and NBI ion losses in the ITER baseline scenario modelled with the Monte Carlo orbit following code ASCOT in a realistic magnetic field including the effect of the plasma response were obtained. The inclusion of the plasma response was found to reduce alpha particle losses but increase NBI losses, with up to 4.2% of the injected power being lost. Additionally, some of the load in the divertor was found to be shifted away from the target plates toward the divertor dome (112).

The effect of external magnetic perturbations on the helical self-organization in nonlinear 3D MHD modelling of fusion plasmas were studied. The same numerical tools have been used to study the Reversed Field Pinches, Tokamak and Stellarator magnetic configurations. Helical magnetic perturbations are confirmed to effectively impact the global helical self-organization of fusion plasmas (113). The neoclassical thermal diffusivity of an axisymmetric toroidal plasma is modified by the effect of RMPs and using a drift-kinetic simulation code the radial thermal diffusivity of ion in the perturbed region was calculated (114). A drift-kinetic δf simulation code was modified for estimating collisional transport in quasi-steady state toroidal plasmas affected by resonant magnetic perturbations and radial electric fields. It was found that radial electron flux is reduced by positive radial-electric fields, although radial diffusion of electron is strongly affected by chaotic field-lines under an assumption of zero electric fields (115). ELM triggering by pellet injection in the DIII-D tokamak has been simulated with the code JOREK with a view to validating its physics models. JOREK modelling results for DIII-D show that the key parameter for the triggering of ELMs by pellets is the value of the localized pressure perturbation caused by pellet injection which leads to a threshold minimum pellet size for a given injection velocity, injection geometry and H-mode plasma characteristics. JOREK has been subsequently applied to evaluate the requirements for ELM control by pellet injection in ITER (116). Simulations with the integrated code TOPICS showed that a small pellet can significantly reduce the ELM energy loss by penetrating deeply into the pedestal and triggering high- n ballooning modes localized near the pedestal top. With injection from the low-field-side, the required conditions are that the speed is fast enough to approach the pedestal top when the pedestal pressure is about 95% of the pressure at the natural ELM onset. The effectiveness of the above suitable conditions of pellet injection for ELM pacing has been confirmed in JT-60U and ITER simulations (117) (118). The code JOREK has been coupled with the resistive wall code STARWALL, which allows to include the effects of eddy currents in 3D conducting structures in non-linear MHD simulations. This allows modelling the plasma dynamics and its interaction with wall currents by solving the MHD equations in realistic toroidal X-point geometry consistently coupled with a model for the vacuum region and the resistive conducting structures. The new simulations show quantitative differences when compared with previous studies and allow the study, among other things, of the dynamics of the locked mode in tokamaks (119). JOREK 3D non-linear MHD simulations of a D2 Massive Gas Injection (MGI) triggered disruptions in JET were performed and compared in detail to experimental data (figure 5). The MGI creates an over density that rapidly expands in the direction parallel to the magnetic field. It also causes the growth of magnetic islands ($m/n=2/1$ and $3/2$ mainly) and seeds the $m/n=1/1$ internal kink mode. O-points of all island chains (including $1/1$) are located in front of the MGI, consistently with experimental observations. The simulated radiation is much below the experimental level, but qualitative agreement is achieved in that the current and thermal quench are observed in the simulations. (120). The stochastisation mechanisms of high-energy Runaway Electron drift orbits were investigated in tokamak plasmas using 3D orbit following codes. The drift resonance was shown to play an important role in determining the onset of stochastic drift orbits for different electron energies, particularly in cases with low-order perturbations that have radially global eigenfunctions of the scale of the plasma minor radius (121). The Runaway Electron generation during tokamak disruptions was investigated by kinetic simulations. Specifically, 3D (2D in momentum space; 1D in the radial direction) Fokker-Planck simulations are coupled with the self-consistent electric field caused by the disruptions. The thermal quench time is varied, and the results are compared with those of the steady-state solution of the runaway generation rate. The hot-tail effect is enhanced when the thermal quench time is shorter than the electron slowing down time (122).

Internal kink instabilities have been studied in straight tokamak geometry employing an electromagnetic gyrokinetic particle-in-cell (PIC) code. The ideal-MHD internal kink mode and the collisionless $m=1$ tearing mode have been successfully simulated with the PIC code (123). Linear simulations using a hybrid model FLUEUTERPE which couples a fluid treatment of electrons with a gyrokinetic treatment of both bulk and fast ions of the internal kink mode in geometry relevant to large tokamak experiments are performed and the effect of gyrokinetic ions considered. It has been demonstrated that the simulated behaviour is consistent with experimental observations of $n=1$, $m=1$ modes destabilised by fast particles (124). Modelling of the QH-mode plasmas shows that a saturated edge peeling-ballooning mode as the possible explanation for the observed Edge Harmonic Oscillation (125). The stability analyses of the ballooning mode with respect to toroidal rotation with the ion diamagnetic drift effect have been performed using the MINERVA-DI code. The stabilizing effect by the ion diamagnetic drift is found to be negligible when the rotation frequency is large compared to the ion diamagnetic drift frequency (126). The influence of the ion diamagnetic flow on the resistive interchange mode including dissipation in the Large Helical Device (LHD) plasmas was investigated with 3D MHD codes. The contribution on the interchange mode stability depends on the difference between the ideal growth rate and the single fluid growth rate including

resistivity and dissipation. When these are close, the ion diamagnetic effects are stabilizing and this can be approximated by an analytic formula. When these are very different the ion diamagnetic effects are destabilizing (127). Two-fluid and the finite Larmor effects on linear and nonlinear growth of the Rayleigh-Taylor instability in a two-dimensional slab were studied numerically with special attention to high-wave-number dynamics and nonlinear structure formation at a low β . The two effects stabilize the unstable high wave number modes for a certain range of the β (128). A cooperation framework for analyses and predictions of the neoclassical toroidal viscosity (NTV) and the resultant toroidal flow was developed among the TOPICS, VMEC and FORTEC-3D codes. It was found that the NTV is one of the torque sources especially in the edge region irrespective of the insertion of the ferritic steel tiles (FSTs) that reduce the toroidal field ripple amplitude and is essential to numerically reproduce the measured toroidal rotation profile in the edge. The up-down asymmetric component of the NTV is damped due to the FSTs and the NTV profile correlates with the profile of the radial electric field (129) (130). The first detailed comparison between gyrokinetic and gyrofluid simulations of collisionless magnetic reconnection has been carried out. Both the linear and nonlinear evolution of the collisionless tearing mode has been analysed. Good agreement between the two approaches over the whole spectrum of linearly unstable wave numbers have been found, both in the drift kinetic limit and for finite ion temperature. Therefore, in the regimes investigated the gyrofluid approach can describe the collisionless reconnection process as well as the more complete gyrokinetic models (131). Nonlinear gyrokinetic simulations of collisionless magnetic reconnection with nonuniformities in the plasma density, the electron temperature, and the ion temperature were performed. It was found that the density gradient can stabilize reconnection due to diamagnetic effects but destabilize driftwave modes that produce turbulence. The electron temperature gradient triggers MTM that drive rapid small-scale reconnection and strong electron heat transport. The ion temperature gradient destabilizes ITG modes that, like the driftwaves, may enhance reconnection in some cases (132). Gyrokinetic simulations of magnetic reconnection were used to investigate plasma heating for strongly magnetized, weakly collisional plasmas. For a low plasma β case, parallel and perpendicular phase mixing strongly enhance energy dissipation yielding electron heating. Heating occurs for a long time period after a dynamical process of magnetic reconnection ended. For a higher β case, the ratio of ion to electron dissipation rate increases, suggesting that ion heating (via phase-mixing) may become an important dissipation channel in high β plasmas (133). Gyrokinetic simulations have found that MTMs are unstable in both spherical tokamaks and large aspect ratio devices. Recent simulations find that MTMs are also unstable in the shallow gradient region just inboard of the MAST H-mode pedestal, which may impact on its evolution between ELMs. The drive for similar MTMs, should be enhanced in the high magnetic shear region of the edge plateau in tokamaks, and perhaps especially in spherical tokamaks. Similar MTMs have also recently been found unstable towards the edge of conventional aspect ratio tokamaks including JET and ASDEX Upgrade, suggesting that this drive mechanism may have wide ranging significance (134). Non-linear local electromagnetic gyrokinetic turbulence simulations of the ITER standard scenario H-mode for the $q = 3/2$ and $q = 2$ surfaces were performed using the self-consistent electromagnetic local gyrokinetic GKW code. The turbulent transport is examined in regions of velocity space characteristic of electrons heated by electron-cyclotron waves. Electromagnetic fluctuations and sub-dominant MTM are found to contribute significantly to the transport of the accelerated electrons, even though they have only a small impact on the transport of the bulk species (135). Linear gyro-kinetic simulations of the classical tearing mode in 3D geometry were performed using the global gyro-kinetic turbulence code, GKW. The results were benchmarked against a cylindrical ideal MHD and analytical theory calculations (136).

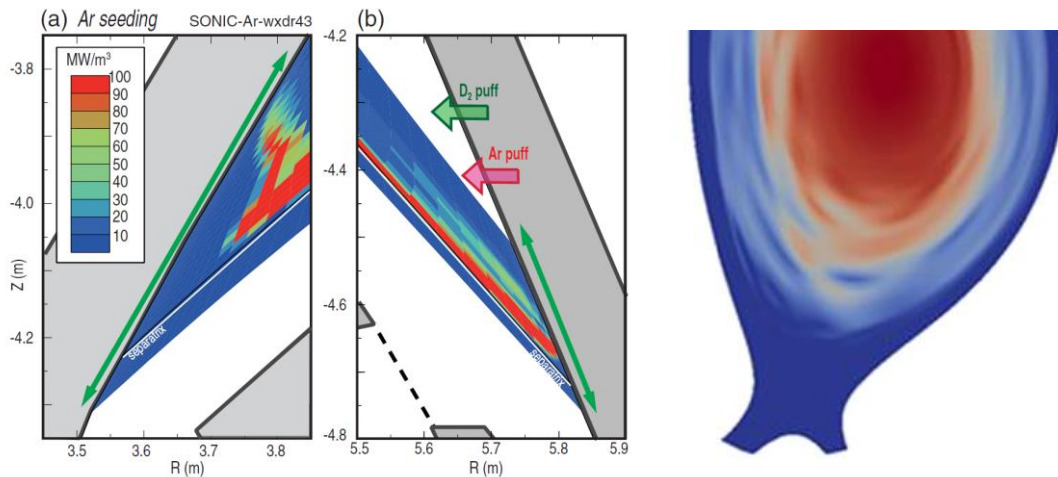


Figure 4 Distributions of Ar radiation power density in the (a) inner divertor and (b) outer divertor plasma detachment simulations of the DEMO divertor (137). Figure 5 Current density at the peak of MHD activity for the JOEUK 3D non-linear MHD simulations of a D2 Massive Gas Injection (MGI) triggered disruptions in JET (138).

The multi-scale interaction of self-consistently driven magnetic islands with electromagnetic turbulence was studied within the 3D, toroidal gyro-kinetic framework. The island is seeded by the electromagnetic turbulence fluctuations, which provide an initial island structure through nonlinear interactions and which grows at a rate significantly faster than the linear tearing growth rate (139). The Self-consistent evolution of the tearing mode in fully kinetic, 3D electromagnetic turbulence showed the highly complex and multi-scale interaction, with turbulence helping magnetic islands to form and grow, while also causing magnetic field line stochasticity and the breakdown of the coherent island structure (140). Simulations of island stabilization by ECCD-driven current have been carried out using the toroidal nonlinear 3D full MHD code XTOR-2F, in which a current source term modeling the ECCD has been implemented. The efficiency parameter has been computed and its variations with respect to source width and location were also computed. The 3D nature of the current source term can lead to the onset of an island if the source term is precisely applied on a rational surface. There was also the observation of a flip phenomenon in which the O- and X-points of the island rapidly switch their position in order for the island to take advantage of the current drive to grow (141). Property of pressure driven modes in LHD

plasmas with a RMP was numerically studied. With the RMP, the pressure driven mode localisation moves to the X-point of the island and the type of the mode structure changes from the interchange type to the ballooning type. This property is attributed to the fact that the equilibrium pressure gradient is larger at the X-point than at the O-point (142) (143).

Fast Particle physics

Fast particle computations focussed on the confinement of fast ions in different scenarios, including the calculation of power loads in ITER due to fast ions with realistic 3D magnetic field taking into account resonant magnetic perturbations, ferritic inserts, blanket modules and MHD perturbations. The kinetic effects of thermal ions on the nonlinear evolution of energetic particle driven MHD modes such as Toroidicity-induced Alfvén Eigenmodes (TAE), and nonlinear simulations of multiple modes in the presence of energetic particles have been also studied in detail. The simulation results were confronted with data from ASDEX-Upgrade, DIII-D, JT-60U, MAST tokamaks and LHD stellarator. In addition, the advances in computation capabilities allowed electromagnetic gyrokinetic simulations of MHD modes, such as TAEs. The physics of EGAMs and the effect of fast ions on sawteeth, Neoclassic Tearing Modes (NTM)s, long-lived mode (LLM) have also been addressed.

The orbit-following Monte Carlo code ASCOT was used to calculate the wall power loads in ITER caused by fusion alphas. The simulations were carried out for a realistic 3D magnetic field that includes the effect of both ferritic inserts and the test blanket modules (144), both causing aberrations in the magnetic field structure particularly at the edge and the power loads in the presence of relevant MHD events. Even with the strongest perturbation, the calculated power load density stays within the design limit of the ITER wall materials. In the case of TAE, while the wall power load density stays at the MHD-quiescent level, significant redistribution of alphas inside the plasma was observed affecting the alpha heating profile (145). Orbit-following simulations were also carried out with the ASCOT code to estimate the alpha particle driven current and torque profiles in ITER baseline scenarios. The total alpha driven torque was found to oppose that generated by the neutral beam injection particles and to be an order of magnitude smaller. Consequently, alpha particles will not significantly contribute to the plasma current nor act as a source of plasma rotation in the ITER baseline scenarios considered (146). MHD instabilities driven by energetic alpha particles and beam deuterium particles were investigated for ITER operation scenarios using a hybrid simulation MEGA code for energetic particles interacting with an MHD fluid. For the ITER steady-state scenario with 9MA plasma current, β -induced Alfvén eigenmodes (BAE modes) with low toroidal mode number ($n = 3, 5$) were found to become dominant in the nonlinear phase although many TAE with $n \sim 15$ are most unstable in the linear phase (figure 6). The redistribution of energetic particles corresponding to 6% and 8% of the central values occur in the nonlinear phase (147). Simulations of DIII-D discharges, shows that the stored beam ion energy is saturated due to Alfvén eigenmodes (AE) at a level lower than in the classical simulation. It was demonstrated that the fast ion spatial profile is significantly flattened due to the interaction with the multiple AE modes (148) (149) (150). The interaction between TAE and energetic ions in LHD was investigated using a reduced version of the MEGA code that implements a realistic equilibrium magnetic field calculated by the HINT code and corresponding TAE calculated by the AE3D code. In the simulations, the linear growth rate of TAE is proportional to the energetic ion density; consequently, the nonlinear saturation level of the TAE amplitude is enhanced by the increase in the energetic ion density (151). A systematic approach to evaluate the linear stability of Alfvén eigenmodes in the presence of fusion-born alpha-particles was developed. Calculation for the ITER baseline scenario showed that the eigenmodes with highest growth rate were found to be core localised TAE with toroidal mode number $n \approx 30$ (152). Multi-mode ITER simulations of TAE, using the nonlinear hybrid HAGIS-LIGKA model were also performed. It was found that the main conclusions from earlier studies of ASDEX-Upgrade discharges can be transferred to the ITER scenario in that global nonlinear effects are crucial for the evolution of the multi-mode scenario (153) and has been showed that nonlinear and non-local effects can influence the mode saturation and thus the energetic Particle transport considerably (154). It was shown that when the plasma β in the core of a tokamak is raised to values of several percent, as required for a thermonuclear fusion reactor, the continuous spectra of long-wavelength slow magnetosonic waves enter the frequency band occupied by continuous spectra of shear Alfvén waves. It was found that these two branches can couple strongly, so that Alfvén modes that are resonantly driven by suprathermal ions transfer some of their energy to sound waves with potentially important consequences for confinement and fusion performance (155). The hybrid code MEGA was used to study the dynamics causing abrupt large-amplitude events (ALE) in beam-driven JT-60U plasmas (156). The resonant excitation of multiple fast-ion-driven Alfvén modes with low toroidal mode numbers $n=1,2,3$ is predicted (157). The growth, nonlinear amplification and chirping dynamics of these modes were analysed numerically using a new orbit-based resonance analysis (ORA) method (158) (159) (160). Simulations of the energetic ion transport from the core of MAST hybrid-like plasmas during long-lived mode (LLM) MHD activity were carried out. The resulting impact on the neutral beam ion deposition and concurrent current drive was modelled using the guiding-centre approximation in the internal kinked magnetic topology (161). Simulations of fast ion populations resulting from MAST neutral beam injection have been applied to MAST $n = 3$ RMP coil configuration. Results show that at low beam energies, particle losses are dominated by parallel transport due to the stochasticity of the field-lines, whereas at higher energies, losses are accredited to the 3D structure of the perturbed plasma and the resulting drifts (162). The impact of rotating magnetic islands on background radial profiles in the presence of strong turbulent transport was analysed, with particular emphasis on island widths of the order of 6–10 ion Larmor radii. A significant reduction of fluctuations is found when island and turbulence co-rotate and the island width is of the order of the radial correlation length of turbulence (163). A new approach to electromagnetic gyrokinetic simulations based on modified gyrokinetic theory and particle-in-cell codes has been used successfully to simulate Toroidal Alfvén Eigenmodes with low perpendicular mode numbers, in the MHD (164). Gyrokinetic particle-in-cell simulations of Alfvén eigenmodes in presence of continuum effects were used to investigate the effect of the bulk plasma temperature on the interplay between the TAE and Kinetic Alfvén Waves (KAWs). A global TAE-KAW structure is identified which appears to be more unstable with respect to the fast ions than a simple (fluid-like) TAE mode (165). A hierarchy of electromagnetic gyrokinetic and fluid hybrid models for simulating global modes has been developed and implemented in the code EUTERPE. The limits of these models were then considered, in simple cases, such as the low shear TAE case, where all models were applicable. Verification against this complete model then permitted more resource efficient parameter scans using the reduced models (166). Comparison of collisionless simulations on global modes (i.e. low poloidal mode number) with the gyrokinetic particle-in-cell code NEMORB against analytical theory and the gyrokinetic semilagrangian code GYSELA was performed (167). The linear dynamics of AE in tokamaks was investigated by means of the code ORB5, within the NEMORB project. A verification and benchmark analysis was performed for

continuum modes in a cylinder and for TAE. Modes in reversed shear equilibrium were also investigated, and the dependence of the spatial structure in the poloidal plane on the equilibrium parameters. In particular, a phase-shift in the poloidal angle was found to be present for modes whose frequency touches the continuum, whereas a radial symmetry was found to be characteristic of modes in the continuum gap (168).

High power H-mode experiments show the extent to which Ion Cyclotron Resonant Heating (ICRH) can be tuned to control sawteeth and NTMs while simultaneously providing effective electron heating with improved flushing of high Z core impurities. Dedicated ICRH simulations using SELFO, SCENIC and EVE, including wide drift orbit effects, explain why sawtooth control is effective with various antenna phasings and show that the sawtooth control mechanism cannot be explained by enhancement of the magnetic shear (169). Energetic particle inertia was incorporated in the MHD momentum equation for the simulation where the beam ion density is comparable to the bulk plasma density. Bump-on-tail type beam ion velocity distribution created by slowing down and charge exchange was considered. It was demonstrated that EGAMs have frequencies higher than the geodesic acoustic modes and the dependence on bulk plasma temperature is weak if energetic particle density is comparable to the bulk plasma density and charge exchange time is sufficiently shorter than the slowing down time to create a bump-on-tail type distribution (170). Finite Larmor radius and finite orbit width effects are studied regarding the excitation of geodesic acoustic modes, showing that these effects are likely to be negligible for sufficiently high concentration of energetic particles, but significant when approaching the threshold of excitation (171).

Development of Heating and Current drive systems

Sophisticated simulations of Heating and Current drive systems focussed on the development of the design of ICRH antennas, with particular emphasis on the application to stellarators and the optimisation of gyrotron components with application to Electron Cyclotron Resonant Heating (ECRH).

Numerical analyses of ICRH antennas have performed the evaluation of the input parameters and of the electric field distribution on the A2 antenna installed on JET and ICRH antennas foreseen for WEST, W7X and ITER experiments (172) (173) (174). Numerical simulations have been performed of the scaled mock-up (1/4) of the proposed W7X ICRF antenna placed in front of dielectric dummy loads. This allows comparing measured and predicted coupling performances and hence validating the electrical design of the antenna. The measurements are compared with the expectations of 3 codes: ANTITER II, MWS and TOPICA. The best agreement is obtained with the BaTiO₃ load for all phasings (175). Detailed SCENIC simulations were performed of a W7X D plasma with 0.5% H minority and with an antenna model close to the design foreseen for the W7X ICRH antenna. A high mirror and a standard equilibrium were considered (figure 7) (176). Extensive simulations of critical gyrotron components have been performed, aiming at the verification of the design of the European gyrotron for ITER (177), and at developments of Multi-frequency designs of 1-2 MW gyrotrons for DEMO (178) (179). Also, an extensive search for parasitic oscillations in several beam tunnel geometries has been done. A key parameter for the gyrotron operation and efficiency is the presence of trapped electrons. Using computer simulations, the influence on the gyrotron operation of the two electron trapping mechanisms that can take place was analysed. Two gun design criteria were then proposed to suppress both mechanisms in order to minimize the risk of possible problems and the performance of three high power gyrotrons prototypes was analysed and compared (180). Finally, efficient simulation tools for the calculation of the energy spread in the electron beam, induced by possible misalignments in coaxial gyrotrons, were developed (181). The interaction between microwaves and wavelength-sized density fluctuations was simulated and quantified using 2-D & 3-D finite difference time domain codes (182) ; these results tell us how heating beams are scattered by plasma turbulence.

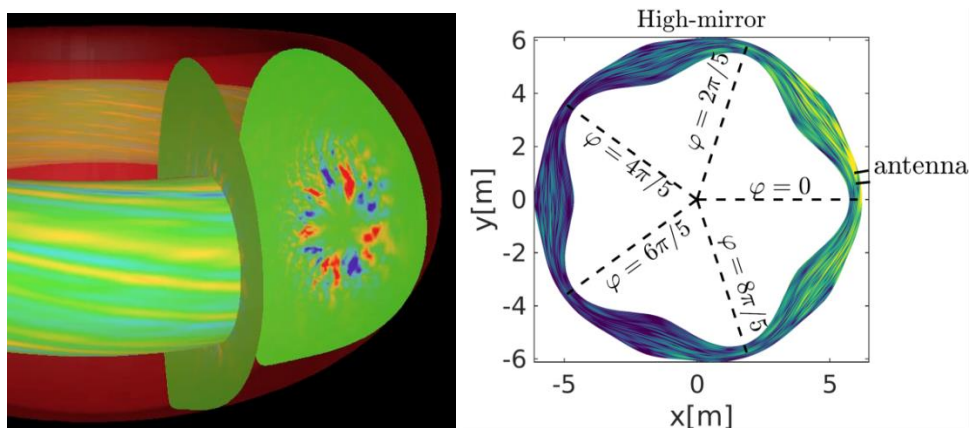


Figure 6 Radial MHD velocity fluctuations of $n = 3-5$ are BAE modes for Steady-state ITER scenario with 9MA plasma current (183). Figure 7 Global wave deposition using a localised antenna design foreseen in W7-X (184).

Development of reactor materials

Reactor Materials studies use mostly Density Functional Theory (DFT) and Molecular Dynamics (MD) calculations to simulate mainly structural but also functional material properties with particular emphasises on the effect of the presence of He on steels and W. DFT calculations of dislocations in transition metals showed that the relative stability of the dislocation core configurations in body-centered cubic (bcc) Fe(He) is profoundly changed by the presence of He. Classical MD and DFT calculations were performed to study the impact of two distinct Fe grain boundaries (GBs) on the clustering properties of He and the possible He effect on GB decohesion. Common properties of He clustering are found for both GBs, which are visibly different from the bcc bulk. In particular, He clusters in the GBs are always elongated in the directions parallel to the interface and contracted in the direction normal to the GB plane, while they are isotropic in the bcc bulk. He is found to decrease GB cohesion, and the embrittling effect of He increases with

its concentration. But interestingly, this effect decreases with He clustering. The present findings are fully compatible with existing experimental evidence, for instance, for a stronger GB embrittlement due to He rather than low temperatures than at higher temperatures (185). The easy, hard and split core configurations of the $\langle 111 \rangle$ screw dislocation and the energy pathways between them were studied in bcc Fe and W using different DFT approaches. All approaches indicate that in Fe, the hard core has a low relative energy, close to or even below that of the saddle configuration for a straight path between two easy cores. The split core configuration is found to be unstable in DFT and of high energy in both Fe and W, in contrast with predictions from most empirical potentials (186). MD simulations have been performed to investigate the effects of irradiated He atoms in W on the bubble nucleation and the dislocation loop formation. Simulation results clearly show that He atoms in W tend to migrate as isolated interstitials at high temperatures and to be absorbed to existing W-vacancies or defects such as bubbles or dislocations. W self-interstitial atoms pushed out from the He bubble tend to stay in the vicinity of the bubble and, then form a dislocation loop when the number of the atoms exceeds the threshold. Since the bubbles and dislocation loops cause further nucleation of bubbles, there appears a He bubble array along $\langle 111 \rangle$ direction. The bubble growth rate within this self-induced bubble growth mechanism will be much faster. Therefore, the interaction between defects in metals and H/He showed that in bulk W, He atoms attract each other into clusters, and the migration barrier for these clusters (at least 3 atoms) is lower than for a single He atom (figure 8) (187). MD simulations of the effects of irradiating thin Fe and FeCr films with ions shows that the damage in bcc Fe in thin films is very different from that in bulk Fe for the same recoil energy. This has consequences for the modelling of irradiation effects. In the quest to develop models that are able to describe neutron damage in the bulk, ion implantation experiments using thin films are often used for validation. These results show that one should carefully account for the effect of free surfaces in these models (188). By means of ab initio calculations combined to statistical mechanics, new evidence that an experimentally undetectable tiny amount of impurities can be responsible for drastic changes in vacancy concentrations ($[V]$), inducing large deviations from an Arrhenius law even at low temperature. It is the case of O and N in α -Fe. These findings are fully compatible with existing experiments, and change the previous common vision that C has the dominant effect. This study provided a route for bridging the long-standing theoretical-experimental gap on the prediction of $[V]$ in metals (189). The properties of point defects resulting from the incorporation of inert-gas atoms in bcc W were investigated systematically using first-principles DFT calculations. The calculations of the interaction of He and other noble-gas atoms with dislocations and nano-defects formed under ion-beam irradiation in Fe and W based alloys showed that the binding energies of a He atom are in excellent agreement with experimental data (190). The interplay between vacancies (V) and interstitial solutes X (X = C, N, and O) and its impact on thermodynamic properties of α -Fe solid solutions were studied. A systematic comparison between the three solutes was performed, investigating X-Fe, X-X, and V-X interactions. In the α -Fe lattice, the strength of X-Fe interactions is found to govern the dissolution properties. Next to vacancies, the competition between solute volume effects and X-Fe interactions results in the preference of all the solutes to occupy off-centered sites. Statistical treatment of the solid solution including these clusters is then achieved by means of low-temperature expansions, checked against Monte Carlo simulations in some specific conditions. Based on the calculation of equilibrium cluster distributions, it is shown that the solubility limit of oxygen in Fe, hardly measurable experimentally, is largely affected by the presence of small V_nO_m clusters (191). Based on a systematic first-principles study, the lowest-energy migration mechanisms and barriers for small vacancy-solute clusters (V_nX_m) were determined in α -Fe for C, N, and O, which are the most frequent interstitial solutes in several transition metals (192). Atomistic studies, which employ both DFT and MD methods, confirmed that the behaviour of vacancies is affected by the presence of H, and vice versa. Changes to H's electronic structure, including a delocalization of charge, are seen at vacancies. Six H atoms can be trapped at a monovacancy; the calculated binding energies are in excellent agreement with experiments. Diffusion paths for H have low barriers giving diffusion coefficients that are in good agreement with experimental data. Significantly reduced vacancy formation energies are seen in areas of high local H concentration, supporting the experimentally observed phenomenon of superabundant vacancy formation and vacancy clustering is clearly enhanced by the presence of significant amount of H atoms. Zero-point energy corrections are important for calculations involving H. This is particularly true when calculating solution energies and H jump barriers, and less so when calculating binding energies (193). Low-energy magnetic states and finite-temperature properties of Cr nanoclusters in bulk bcc Fe and Fe nanoclusters in bulk Cr were investigated using DFT and the Heisenberg-Landau Hamiltonian based magnetic cluster expansion (MCE). It was shown, by means of noncollinear magnetic DFT calculations, that magnetic frustration caused by competing ferromagnetic and antiferromagnetic interactions either strongly reduces local magnetic moments while keeping collinearity or generates noncollinear magnetic structures (194) (195). Studies of the H interaction with Be surfaces and its effect on the energetics of various closed packed surfaces show that adsorbed H atoms repulsively interact with each other; stretch the Be surface and, nearly in all cases, result in the reduction of the surface energy (196). The optimal dumbbell configurations and optimized further migration paths were calculated Al_2O_3 (corundum) crystals by simulating all possible O_i migration trajectories, with the large-scale hybrid DFT-LCAO PBE0 calculations on $2 \times 2 \times 1$ supercells of defective α - Al_2O_3 crystals using the CRYSTAL14 computer code. The limiting barrier height for oxygen interstitial 3D migration was estimated as 1.3 eV (197).

Reactor Technologies

Reactor technology studies focus mainly on fluid flows for vacuum applications and neutronics calculations. The effect of the Reynolds number on scalar structures for flow in a cylindrical pipe with Reynolds number up to 40,000 have been compared with previous results and good agreement was found. Details on the turbulent quantities such as the mean flow, turbulent stresses, turbulent kinetic energy budget, and the turbulent statistics were obtained (198). Steady half-space single gas flow driven by an adsorbing planar wall was investigated based on the solution of the BGK kinetic model. It has been found that as the gas thermal accommodation on the surface is reduced for the prescribed adsorbing flux, the sticking coefficient must be increased to sustain the prescribed flux or otherwise for the same sticking coefficient the adsorbing flux is reduced. This behaviour is further enhanced as the difference, between the surface and the far upstream temperatures, is increased, which is commonly the case in cryogenic applications (199). An integrated software tool for modeling and simulation of complex gas distribution systems operating under any vacuum conditions was developed and validated. Detailed calculations were performed of the flow patterns and paths in the ITER cassettes, in the gaps between the cassettes and along the divertor ring, as well as of the total throughput for various pumping scenarios and dome pressures (figure 9) (200). Neutronics calculations aimed at the comparison of various blanket module DEMO concepts were performed in order to improve reactor safety (201); calculations aiming at understanding ITER port shutdown dose

rates were performed (202) (203) (204) (205) and ITER Diagnostic Port Plugs were successfully modelled resulting in the optimal shielding configuration (206) (207) (208). The IFMIF (International Fusion Material Irradiation Facility) test cell design has been developed and optimized based on the existing modular test cell concept. According to preliminary neutronic calculation results performed for the design of the IFMIF test cell design, limited access to the quench tank area for maintenance after beam shut-off can be expected with the current arrangement (209) (210) (211). Shielding performances analysis for the IFMIF test facility based on high-fidelity Monte Carlo neutronic calculations was carried out with very detailed analyses in order to examine the neutron streaming effect caused by pipe penetrations and gaps around removable shielding plugs of the IFMIF Test Cell (212). The effective dose rate expected during the Linear IFMIF Prototype Accelerator (LIPAc) injector commissioning was analysed by a Monte Carlo calculation and compared with the measured value. The yield obtained was smaller than previously reported in a literature by a factor of a few and seems to depend on some beam conditions, and the calculations provided a conservative estimate (213).

Conclusions

The use of the Helios computer has been rather successful with a large scientific output expressed in the number of peer-reviewed publications of around 1 per project per year. In the 5th Cycle of operation of Helios, over 120 projects have been selected, corresponding to over 300 users. Projects included the development of a number of novel numerical techniques that were tested on Helios. The developments focussed mainly on noise reduction in particle in cell based algorithms and improvements in the collision operators. Most computation resources were devoted to plasma turbulence studies. Plasma turbulence simulations have moved towards full torus calculations with more detailed comparisons with experimental data and the inclusion of more sophisticated models for the electromagnetic effects, real ion-to-electron mass ratio, role of fast ions, momentum transport, the role of GAMs, electron dynamics and 3D effects with applications to Tokamaks and Stellarators. On the other hand, significant resources were devoted to other topics, including technology related applications. Edge physics simulations focused on the SOL and turbulence simulations have clarified the relative role of the resistive ballooning modes, drift waves, and ITG modes in the SOL. MHD simulations focussed on the study of ELMs, disruptions and generation of runaway electrons, together with the analysis of kink, peeling and ballooning modes, Rayleigh-Taylor instabilities, MTM, tearing modes, collisionless magnetic reconnection and NTV. Fast particle computations focussed on the confinement of fast ions in different scenarios, including the calculation of power loads in ITER due to fast ions with realistic 3D magnetic field taking into account resonant magnetic perturbations, ferritic inserts, blanket modules and MHD perturbations. Sophisticated simulations of Heating and Current drive systems focussed on the development of the design of ICRH antennas, with particular emphasis on the application to stellarators; and the optimisation of gyrotron components with application to ECRH. Reactor Materials studies use mostly DFT and MD calculations to simulate mainly structural but also functional material properties. Reactor technology studies focussed mainly on fluid flows for vacuum applications and neutronic calculations. At the end of its life cycle the use of Helios will be replaced in Europe with a new EUROfusion supercomputer, allowing further development of fusion technologies based on computer modelling and simulations.

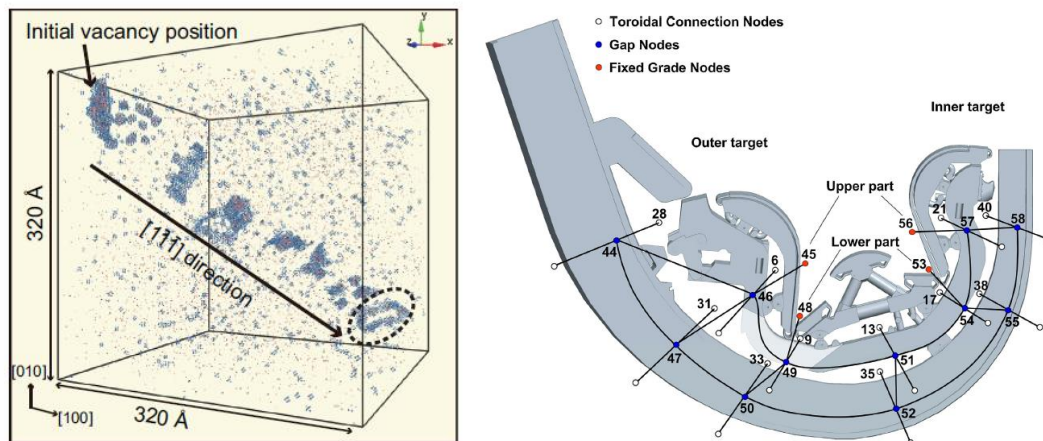


Figure 8 Atomic configuration at 2000 K after 6 ns from the random distribution of He atoms is shown for MD simulations performed to investigate the effects of irradiated He atoms in W on the bubble nucleation and the dislocation loop formation. The leading dislocation loop is indicated by a broken circle (214). Figure 9 Schematic presentation of the pipe network approximating the geometry of the actual gas flow between ITER adjacent cassettes in the toroidal direction along the divertor ring and through the gaps between the cassettes facing the plasma side (215).

Acknowledgments

This work has been carried out within the framework of the EUROfusion Consortium and has received funding from the Euratom research and training programme 2014-2018 under grant agreement No 633053. The views and opinions expressed herein do not necessarily reflect those of the European Commission.

References

1. Kang, Lecture Notes in Comput. Sci. & Eng, vol.98, 789-797, 2. Idomura, Comput. Sci. Disc 5, 014018 (2012), 3. Idomura et al, Int. J. HPC Appl. 28, 73 (2014), 4. Idomura et al, Plasma Fusion Res. 9, 3503028 (2014), 5. Satake et al, PFR 3 (2008) S1062, 6. Kleiber et al Comput Phys. Commun. 182 (2011) 1005, 7. Matsuoka et al Comp. Phys. Commun. 185 (2014) 2313–2321, 8. McMillan et al. PoP 21 052501 (2014), 9. Kiviniemi et al Comp. Phys. Commun. 203 (2016) 162–167, 10. Nakata et al Comp. Phys. Commun. 197 (2015) 61–72, 11. Nunami et al. PFR 10 1403058 (2015), 12. Estève et al, PoP 22 (2015) 122506, 13. Stegmeir et al Comp. Phys. Commun. 198 (2016) 139–153, 14. Mishchenko et al. PoP 21 092110 (2014),

15. Kleiber et al. PoP 23 032501 (2016), 16. Maeyama et al Comp. Phys. Commun. 184 (2013) 2462–2473, 17. Pfefferlé et al Comp. Phys. Commun. 185 (2014) 3127–3140, 18. T. Görler, et al, PoP 23, 072503 (2016), 19. Hatch et al. PoP 20 012307 (2013), 20. Maeyama et al. PFR 9 1203020 (2014), 21. Maeyama et al. PoP 21 052301 (2014), 22. Maeyama et al. PRL 114 255002 (2015), 23. Wilkie et al. JPP (2015) 905810306, 24. Afeyan et al. EPJ (2014), 25. Vernay et al. PPCF 55 (2013) 074016, 26. Idomura, J. Comput. Phys. 313, 511 (2016), 27. Idomura, Plasma Fusion Res. 11, 2403006 (2016), 28. Villard et al, J. Phys Conf. Ser. 561 (2014) 012022, 29. Asahi et al. PoP 21 052306 (2014), 30. Teaca et al. PoP 21 072308 (2014), 31. Dominski et al. PoP 22 062303 (2015), 32. Matsuoka et al. PoP 22 072511 (2015), 33. Yagi et al. Contrib. Plasm. Phys. 54, No. 4-6, 363–367 (2014), 34. Yagi et al. PFR 9 3403030 (2014), 35. Miyato PFR 9 1203148 (2014), 36. Watanabe et al. PoP 22 022507 (2015), 37. Ball et al. PPCF 58 (2016) 045023, 38. Ball et al. PPCF 56 (2014) 095014, 39. Idomura, Phys. Plasmas 21, 022517 (2014), 40. Pueschel et al. PRL 110 155005 (2013), 41. Pueschel et al. PoP 20 102301 (2013), 42. Nakata-Idomura, Nucl. Fusion 53, 113039 (2013), 43. Idomura-Nakata, Phys. Plasmas 21 020706 (2014), 44. Oberparleiter et al. PoP 23 042509 (2016), 45. Strugarek et al, PRL 111 (2013) 145001, 46. Zarzoso et al, PRL 110 (2013) 125002, 47. Abdoul et al. PPCF 57 (2015) 065004, 48. Nunami et al. PFR 8 1203019 (2013), 49. Poyé et al. PoP 22 030704 (2015), 50. Predebon et al. PoP 22 042513 (2015), 51. Carmody et al. PoP 22 012504 (2015), 52. Ishizawa et al. PoP 21 055905 (2014), 53. Ishizawa et al. NF 55 (2015) 043024, 54. Xanthopoulos et al. PRL 113 155001 (2014), 55. Xanthopoulos et al, Phys. Rev. X 6, 021033, 56. Velasco et al PPCF 58, 084004 (2016), 57. Proll et al. PoP 20 (2013) 12506, 58. Pedrosa et al. NF 55 (2015) 052001, 59. Citrin et al. PPCF 57 014032 (2015), 60. Garcia et al. NF 55 (2015) 053007, 61. Tegnered et al. PPCF 58 (2016) 045021, 62. D. Told et al. PoP 20, 122312 (2013), 63. Görler et al. PoP 21 122307 (2014), 64. Navarro et al. PoP 22 042513 (2015), 65. Doerk et al. PoP 22 042503 (2015), 66. Hatch et al. NF 55 (2015) 063028, 67. Dif-Pradalier et al. Phys. Rev. E 82 025401(R) (2010), 68. Dif-Pradalier et al. PRL 114 085004 (2015), 69. Merlo et al. PPCF 57 (2015) 054010, 70. Gurchenko et al. EPL 110 55001 (2015), 71. Gurchenko et al. PPCF 58 (2016) 044002, 72. Korpilo et al Comp. Phys. Commun. 203 (2016) 128–137, 73. Niskala et al. NF 55 (2015) 073012, 74. Hillesheim et al. PPCF 58 (2016) 014020, 75. McMillan PoP 22 020707 (2015), 76. Yoshida et al. NF 55 (2015) 073014, 77. Villard et al. PPCF 55 (2013) 074017, 78. Wakatsuki et al. PPCF 57 (2015) 065005, 79. Afeyan et al. EPJ (2014), 80. Maeyama et al. PRL 114 255002 (2015), 81. Wiesen et al. JNM 463 (2015) 480–484, 82. Masetto et al. PoP 20 092308 (2013), 83. Masetto et al. PoP 22 012308 (2015), 84. Ricci et al, PPCF 54 124047 (2012), 85. Ricci and Rogers, Phys. Plasmas 20 010702 (2013), 86. Jolliet et al. PoP 21 022303 (2014), 87. Anderson et al. PoP 21 122306 (2014), 88. Halpern et al. PoP 21 022305 (2014), 89. Fasoli et al. 2006 Phys. Plasmas 13 055902, 90. Riva et al. PPCF 58 (2016) 044005, 91. Zweben et al. 2009 Phys. Plasmas 18 082505, 92. Halpern et al. PPCF 57 (2015) 054005, 93. Tskhakaya et al. FED 463 (2015) 624–628, 94. Tskhakaya et al. PoP 23 032128 (2016), 95. Halpern et al. NF 53 122001 (2013), 96. Hoshino et al. JNM 463 (2015) 573–576, 97. Hoshino et al. PFR 9 3403070 (2014), 98. Asakura et al. NF 53 (2013) 123013, 99. Wersal et al. NF 55 (2015) 123014, 100. Tskhakaya et al. 15th International Workshop on Plasma Edge Theory in Fusion Devices Nara, Japan (2015), 101. Loizu et al. PoP 21 062309 (2014), 102. Brida et al. Contrib. Plasm. Phys. 54 No. 4-6, 469–473 (2014), 103. Moulton et al. PPCF 55 (2013) 085003, 104. Krebs et al. PoP 20 082506 (2013), 105. Huijsmans et al. NF 53 (2013) 123023, 106. Orain et al. PoP 20 102510 (2013), 107. Orain et al. PPCF 57 (2015) 014020, 108. Orain et al. PRL 114 035001 (2015), 109. Pamela et al. PPCF 55 (2013) 095001, 110. Pamela et al. 2015 PPCF 58 014026, 111. Becoulet et al. PRL 113 115001 (2014), 112. Varje et al. NF (2016) 046014, 113. Bonfiglio et al. PPCF 57 (2015) 044001, 114. Kanno et al. PPCF 55 (2013) 065005, 115. Kanno et al. Contrib. Plasm. Phys. 1–6 (2016), 116. Futatani et al. NF 54 073008 (2014), 117. Hayashi et al. NF 53 (2013) 123009, 118. Hayashi et al. Contrib. Plasm. Phys. 54 No. 4-6, 599–604 (2014), 119. Hoelzl et al. J. Phys. Conf. Ser. 561 (2014) 012011, 120. Fil et al. PoP 22 062509 (2015), 121. Matsuyama et al. NF 54 (2014) 123007, 122. Nuga et al. PFR 10 1203006 (2015), 123. Mishchenko et al. PoP 19 122104 (2012), 124. Cole et al. PoP 21 072123 (2014), 125. Liu NF 55 113002 (2015), 126. Aiba PPCF 58 (2016) 045020, 127. Nicolas et al. PFR 10 3403018 (2015), 128. Goto et al. PoP 22 032115 (2015), 129. Honda et al. NF 54 (2014) 114005, 130. Honda et al. NF 55 (2015) 073033, 131. Zacharias et al. PoP 21 062106 (2014), 132. Kobayashi et al. PoP 21 040704 (2014), 133. Numata et al. JPP 305810201 (2015), 134. Dickinson et al. PPCF 55 (2013) 074006, 135. Casson et al. NF 55 (2015) 012002, 136. Hornsby et al. PoP 22 022118 (2015), 137. Asakura et al. NF 53 (2013) 123013, 138. Fil et al. PoP 22 062509 (2015), 139. Hornsby et al. PPCF 57 (2015) 054018, 140. Hornsby et al. PPCF 58 (2015) 014028, 141. Février et al. PPCF 58 (2016) 045015, 142. Ichiguchi et al. PFR 9 3403134 (2014), 143. Ichiguchi et al. NF 55 (2015) 073023, 144. Äkäslompolo et al. NF 55 (2015) 093010, 145. Snicker et al. NF 53 (2013) 093028, 146. Snicker et al. NF 55 (2015) 063023, 147. Todo et al. PFR 9 3403068 (2014), 148. Todo et al. NF 54 (2014) 104012, 149. Todo et al. NF 55 (2015) 073020, 150. Todo et al. NF 56 (2016) 112008, 151. Nishimura et al. PFR 8 2403090 (2013), 152. Rodrigues et al. NF 55 (2015) 083003, 153. Schneller et al. PPCF 58 014019 (2016), 154. Lauber et al. PPCF 57 05401(2015), 155. Bierwage et al. PRL 114 015002 (2015), 156. Bierwage et al. NF 53 (2013) 073007, 157. Bierwage et al. NF 54 (2014) 104001, 158. Bierwage et al. PoP 21 112116 (2014), 159. Bierwage et al PoP 23 042511 (2016), 160. Bierwage et al PoP 23 042512 (2016), 161. Pfefferle et al. NF 54 (2014) 064020, 162. Pfefferle et al. NF 55 (2015) 012001, 163. Zarzoso et al. NF 55 (2015) 113018, 164. Mishchenko et al. PoP 21 052113 (2014), 165. Mishchenko et al. PoP 21 052114 (2014), 166. Cole et al. PPCF 57 (2015) 054013, 167. Biancalani et al. NF 54 (2014) 104004, 168. Biancalani et al. PoP 23 012108 (2016), 169. Graves et al. PPCF 57 (2015) 014033, 170. Wang et al. PoP 22 092507 (2015), 171. Zarzoso et al. NF 54 (2014) 103006, 172. Mayoral et al. NF 54 (2014) 033002, 173. Helou et al. FED 96–97 (2015) 473–476, 174. Dumortier et al. AIP Conf. Proc. 1580, 362 (2014), 175. Dumortier et al. FED 96–97 (2015) 463–467, 176. Faustin et al. PPCF 58(7) 2016, 177. Avramidis et al, 41th International Conference on Infrared, Millimeter, and Terahertz waves (IRMMW-THz), 2016, 178. Franck et al. 40th Int. Conf. IRMMW-THz, 2015, 179. Kalaria et al, 17th IEEE International Vacuum Electronics Conference (IVEC), 2016, 180. Pagonakis et al. PoP 23 023105 (2016), 181. Franck, et al, IEEE Trans. Electron Devices, DOI:10.1109/TED.2016.2592533, (2016), 182. Köhn et al. PPCF 58 105008 (2016), 183. Todo et al. PFR 9 3403068 (2014), 184. Faustin et al. PPCF 58(7) 2016, 185. Zhang et al. JNM 459 (2015) 247–258, 186. Ventelon et al. Acta Mater. 61 11 (2013) 3973–3985, 187. Kobayashi et al. JNM 463 (2015) 1071–1074, 188. Aliaga et al. Acta Mater. 101 (2015) 22–30, 189. Schuler et al. PRL 115 015501 (2015), 190. Nguyen-Manh et al. Nucl. Instrum. Meth. B 352 (2015) 86–91, 191. Barouh et al. Phys. Rev. B 90 054112 (2014), 192. Barouh et al. Phys. Rev. B 92 104102 (2015), 193. Hayward et al. Phys. Rev. B 87 174103 (2013), 194. Nguyen-Manh et al. Annals of Nuclear Energy, 77, 246-251 (2015), 195. Fu et al. Phys. Rev. B 91 094430 (2015), 196. Bachurin and Vladimirov FED Available online 20 December 2015, 197. Zhukovskii et al. Nucl. Instrum. Meth. B 374 (2016) 29–34, 198. Satake et al. FST 68 3 (2015) 640-643, 199. Tantos et al. Vacuum (2015), 200. Vasileiadis et al. FED 103 (2016) 125–135, 201. Juárez et al. FED online 24 November 2015, 202. Turner FED 96–97 (2015), 203. Serikov et al. FED 87 (2012) 690–694, 204. Serikov et al. FED 88 (2013) 1965–1968, 205. Serikov et al. FED 89 (2014) 1964–1968, 206. Pampin FED online 12 January 2016, 207. Juárez et al. FED 100 (2015) 501-506, 208. Juárez et al. FED 101 (2015) 67-72, 209. Tian et al. FED 98–99 (2015) 2085–2088, 210. Tian et al. FED 88 (2013) 635–639, 211. Tian et al. FED 89 (2014) 1694–1698, 212. Kondo et al. FED 98-99 (2015) 1998-2002, 213. Kondo et al. FED (2016), 214. Kobayashi et al. JNM 463 (2015), 1071–1074, 215. Vasileiadis et al. FED 103 (2016) 125–135.